

Denoising of 3-D Magnetic Resonance Images Using a Residual Encoder-Decoder Wasserstein Generative Adversarial Network

Maosong Ran¹, Jinrong Hu², Yang Chen³, Hu Chen¹, Huaiqiang Sun⁴, Jiliu Zhou¹, Yi Zhang^{1,*}

1. College of Computer Science, Sichuan University, Chengdu 610065, China
2. Department of Computer Science, Chengdu University of Information Technology, Chengdu 610225, China
3. Lab of Image Science and Technology, Southeast University, Nanjing 210096, China
4. Department of Radiology, West China Hospital of Sichuan University, Chengdu 610041, China

* Corresponding author, yzhang@scu.edu.cn

Abstract—Structure-preserved denoising of 3-D magnetic resonance images (MRI) is a critical step in the medical image analysis. Over the past years, many algorithms have been proposed with impressive performances. Inspired by the idea of deep learning, in this paper, we introduce a MRI denoising method based on the residual encoder-decoder Wasserstein generative adversarial network (RED-WGAN). Specifically, to explore the structure similarity among neighboring slices, 3-D configuration are utilized as the basic processing unit. Residual autoencoder, combined with deconvolution operations are introduced into the generator network. Furthermore, to alleviate the shortcoming of traditional mean-squared error (MSE) loss function for over-smoothing, the perceptual similarity, which is implemented by calculating the distances in the feature space extracted by a pre-trained VGG-19 network, is incorporated with MSE and adversarial losses to form the new loss function. Extensive experiments are studied to access the performance of the proposed method. The experimental results show that the proposed RED-WGAN achieves superior performance relative to several state-of-art methods in both simulated and clinical data. Especially, our method demonstrates powerful ability in both noise suppression and structure preservation.

Index Items—Magnetic resonance images (MRI); Image Denoising; Deep Learning; Wasserstein GAN; Perceptual Loss.

1 Introduction

Magnetic resonance imaging (MRI) is a non-invasive high-resolution imaging modality and it plays a very important role in current clinical diagnosis and scientific research procedures as it can reveal the 3D internal details and structures of tissues and organs in the human body [1,2,3]. However, the quality of MR images can be easily affected by noise during the procedure of image acquisition, especially when high-speed and high resolution is needed. The noise in MR image can not only degrade the imaging quality and the accuracy of clinical diagnoses, but also has negative influences on the reliability of subsequent analytic tasks such as registration, segmentation and detection. As a result, efficient algorithms of noise reduction are necessitous for the further MR analysis.

Over the past years, a wide variety of post-processing MRI denoising methods have been developed to improve the imaging quality of MR images [1,2,3]. These methods are fall into three categories: (a) filtering based methods [2,4,5,6], (b) domain transform based methods [7,8] and (c) statistical methods [9,10]. The filtering based methods is the most direct methods and denoise the MR images in spatial domain. Mc Veigh et al. [4] investigated results of denoised MR images with both spatial and temporal filters. Most typically, Perona and Malik [5] proposed the classical PM model with a multiscale smoothing and edge detection scheme called anisotropic diffusion filter. It utilizes gradient information to extract the image structures while reducing the noise. PM filter and its variants have been successfully extended to 2D and 3D MR images [6,11,12,13]. Different from the denoising methods in spatial domain, reducing noise in a transformed domain is also widely researched and some typical methods include wavelet and discrete cosine transform (DCT) based methods [7,8,14,15,16,17]. The statistical approaches first estimate the parameters of Rician noise in noisy MR images. After that, the results are used to yield statistically optimal denoised image [18,19,20,21].

Recently, the methods based on self-similarity and sparsity of image have attracted much attention in the field of noise reduction for MRI images. Most algorithms originate from the famous nonlocal means (NLM) filter [22], which estimates current pixel by weighted averaging its similar patches in a search window. One critical drawback of NLM filter is that it is time-consuming to find similar patches. Several variants of NLM filters have been extensively studied to improve this issue for MR Rician denoising [2,23,24,25,26]. Specifically, in [23], the authors proposed a fast 3D optimized blockwise version of NLM (ONLM) filter to reduce the computational complexity. In order to simultaneously make full use of the self-similarity and sparsity of images, the authors in [26] combined the 3D DCT hard thresholding method and 3D rotationally invariant version of the nonlocal means filter, which achieved a competitive result. In addition, another state-of-the-art denoising method based on patches is the block-matching and 3D (BM3D) filter [27], which combines the ideas of nonlocality and domain, transform [14]. It first groups the similar patches into a 3D array, then transforms the array into

frequency domain using DCT or wavelet, and finally averages multiple estimates at each location. In [28], the authors adopted the BM3D to process volumetric data called BM4D and achieved state-of-the-art performances. Another method similar to BM3D is higher-order singular value decomposition (HOSVD) [29], which also imposes machine learning technique for noise reduction [3]. The differences between BM4D and HOSVD is that the bases of HOSVD are learned from images, which are more adaptive than analytical transforms.

In recent years, the explosive development of deep learning (DL) suggests a kind of new methods for image processing and computer vision [30,31,32]. Except for the extensive researches in high-level tasks, such as image analysis [33,34], deep learning has been introduced into low-level tasks, including image denoising, deblurring and super-resolution [35,36,37,38,39]. Autoencoder, multilayer perception and convolutional neural network (CNN) were respectively used for image restoration and achieved competitive results with some state-of-art methods, such as BM3D, NLM and sparse representation [36]. In the field of medical imaging, some pioneering works are given in [40,41,42,43,44,45,46]. However, to our best knowledge, the researches for MRI denoising is quite limited and the only work for MRI denoising is represented in [47]. The authors proposed a simple plain CNN for MRI denoising.

Despite the extensive researches for MRI denoising, current methods suffer from several shortcomings, for examples, computational burden, non-convex optimization and/or parameter selection, which seriously impede the applications of these methods in practice. To conquer these problems and fully explore the potential of latest techniques in deep learning, in this paper, we propose a MRI denoising method based on the residual encoder-decoder Wasserstein generative adversarial network (RED-WGAN). The contributions of this paper are fivefold: (a) the proposed model is based on the WGAN framework, which has demonstrated powerful ability to learn the data distribution in a low dimensional manifold; (b) the ideas of residual network and autoencoder are imposed to maintain the structural details and edges, which are clinically important; (c) to mitigate the drawback of traditional mean-squared error (MSE) loss function, the perceptual similarity is incorporated with MSE and adversarial losses to form a new loss function; (d) with a proper training procedure, our method yields competitive results with several state-of-art methods; and (e) it is highly computationally fast, and well compatible for parallel implementation on graphic processing units (GPUs).

The rest of this paper is organized as follows. The proposed method is described in Section II. The experiments and evaluation are given in Section III. Finally, the discussion and conclusion are drawn in section IV.

2 Methods

2.1 Noise Reduction Model

One difficulty of MRI denoising is that magnitude images, which are constructed by the real and imaginary parts, are the common form in MRI [48]. The noise in magnitude images obeys Rician distribution which is much complex than traditional additive noise such as Gaussian and impulse noise. Many methods were given to statistically model the degradation procedure and the accuracy of model heavily affects the final denoising results. DL is an effective way to circumvent this problem, which ignores the physical process and models this procedure corruption by learning from the samples.

The aim of MRI denoising is to recover a high-quality MR image from the corresponding noisy MR image. Let $\mathbf{x} \in \mathbf{R}^{m \times n}$ denote a noisy MR image and $\mathbf{y} \in \mathbf{R}^{m \times n}$ denote the corresponding noise-free MR image. The relation between them can be represented as:

$$\mathbf{x} = \sigma(\mathbf{y}) \quad (1)$$

where σ is a mapping function denoting the procedure of noise contamination. Because the DL-based method is a black box and independent from the statistical characteristic of the noise, the MR denoising can be simplified to seek the optimal approximation of function σ^{-1} and the denoising procedure can be formulated as:

$$\arg \min_f \|\hat{\mathbf{y}} - \mathbf{y}\|_2^2 \quad (2)$$

where $\hat{\mathbf{y}} = f(\mathbf{x})$ which is the estimation of \mathbf{y} and f denotes the optimal approximation of σ^{-1} .

2.2 Wasserstein GAN

From the viewpoint of statistics, \mathbf{x} and \mathbf{y} can be regarded as two samples from two different data distribution, noisy image distribution P_n and noise-free image distribution P_r respectively. Then the denoising operation is a mapping procedure which transforms one distribution to another, that is, the function f maps the samples from P_n to another certain distribution P_g which is close to P_r .

Generative adversarial network (GAN) [49] is a kind of generative model which comprised of two components: generative model G and discriminative model D . GAN has been widely applied in many fields such as image super-resolution [35], image modality transform [50] and image generation [51]. The role of discriminative model is to determine whether a sample is from the generative model distribution P_g or the real data distribution P_r , and the generative model generates new sample from the input sample and try to make the new sample satisfy the real data distribution P_r as much as

possible.

The training process of GAN is a minimax game with the following loss function $L(D, G)$ as

$$\min_G \max_D L(D, G) = E_{x \sim P_r} [\log D(x)] + E_{z \sim P_n} [\log (1 - D(G(z)))] \quad (3)$$

To solve Eq. (3), G and D are optimized alternatively.

In [53], the authors proved that the training of GAN is difficult, because Eq. (3) may lead to vanishing gradient of generator G when the discriminator D is fixed. To avoid this problem, a variant of GAN was proposed by Martin et al., which is titled as Wasserstein GAN (WGAN) [54] and achieves significant improvement. Furthermore, Gulrajani et al. presented an improved version of WGAN with gradient penalty to accelerate the convergence [55]. The changes on loss function are as follows:

$$L_{WGAN}(D) = -E_{x \sim P_r} [D(x)] + E_{z \sim P_n} [D(G(z))] + \lambda E_{\hat{x} \sim P_{\hat{x}}} [(\|\nabla_{\hat{x}} D(\hat{x})\|_2 - 1)^2] \quad (4)$$

where the last term is a gradient penalty factor, λ is a penalty coefficient, $P_{\hat{x}}$ is a distribution which samples uniformly along straight lines between pairs of points sampled from the real data distribution P_r and generator distribution P_g . The loss function of generator G is formulated as:

$$L_{WGAN}(G) = -E_{z \sim P_n} [D(G(z))] \quad (5)$$

2.3 Combined Loss Function

MSE is the most typical loss function for pixel-level transform tasks, which minimizes pixel-wise differences between ground truth image and generated image. It can be calculated as:

$$L_{MSE}(G) = \frac{1}{WHD} \|G(z) - y\|^2 \quad (6)$$

where W, H, D stands for the dimensions of the image, respectively. Recent studies suggest that although MSE loss can achieve high peak signal to noise ratio (PSNR), it may suffer from loss of details, especially high-frequency details, which have serious impact on clinical diagnosis [35].

To efficiently handle this problem, a perceptual loss is involved into the proposed loss function [55,56,57]. A pre-trained network can be utilized to extract the features from the ground truth and generated images. The difference between the features from ground truth and generated image are treated as the perceptual similarity. Then the perceptual loss function be defined as follows:

$$L_{Perceptual}(G) = \frac{1}{WHD} \|F(G(z)) - F(x)\|_F^2 \quad (7)$$

where F is a feature extractor, W, H, D stands for the dimensions of feature maps. In this paper, we apply the pre-trained

VGG-19 network [58] to extract the features of image. The VGG-19 network contains 19 layers: the first 16 layers is convolutional layers and the subsequent 3 layers is fully-connected layers. We only use the first 16 layers as our feature extractor. Then the specific perceptual loss based on VGG network is employed as follows

$$L_{VGG}(G) = \frac{1}{WHD} \|VGG(G(z)) - VGG(x)\|_F^2 \quad (8)$$

Then we obtain the joint loss function of generator G as a weighted form, which consists of MSE loss, VGG loss and discriminator loss.

$$L_{RED-WGAN} = \lambda_1 L_{MSE}(G) + \lambda_2 L_{VGG}(G) + \lambda_3 L_{WGAN}(G) \quad (9)$$

2.4 Network Architectures

The overall architecture of the proposed RED-WGAN network is illustrated in Fig.1. It consists of a generator network G , a discriminator network D and a VGG network as the feature extractor. The specific structure of generator network G is demonstrated in Fig.2. To accelerate the training procedure and preserve more details, short connections and deconvolution layers are introduced. Furthermore, to explore the ability of autoencoder to deal with noisy samples, the convolution and deconvolution layers are symmetrically arranged. Specifically, the generator G is with a encoder-decoder structure, which is made up of 8 layers, including 4 convolutional and 4 deconvolutional layers. Short connections link the corresponding convolution-deconvolutional layer-pairs. Except the last layer, the other layers perform 3-D convolution, batch-normalization and leaky ReLU operation in sequence and the last layer only performs 3-D convolution and leakyReLU operation. In this paper, all kernels are set to $3 \times 3 \times 3$ and the number of filters are 32, 64, 128, 256, 128, 64, 32, 1 in sequence.

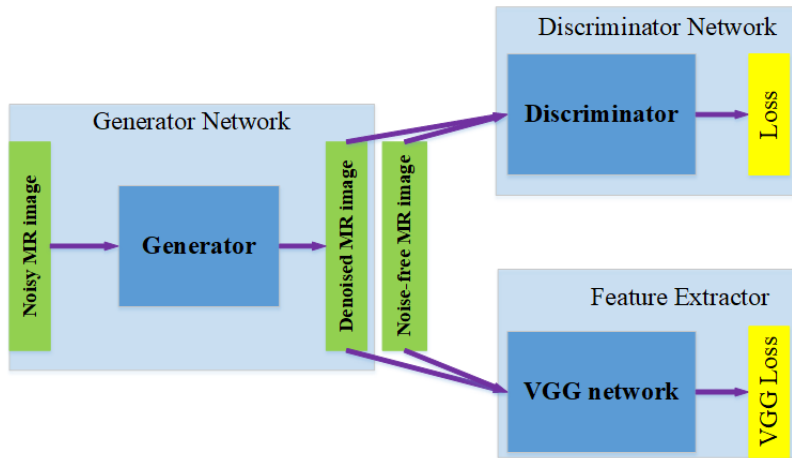


Fig. 1. Overall architecture of our proposed RED-WGAN network

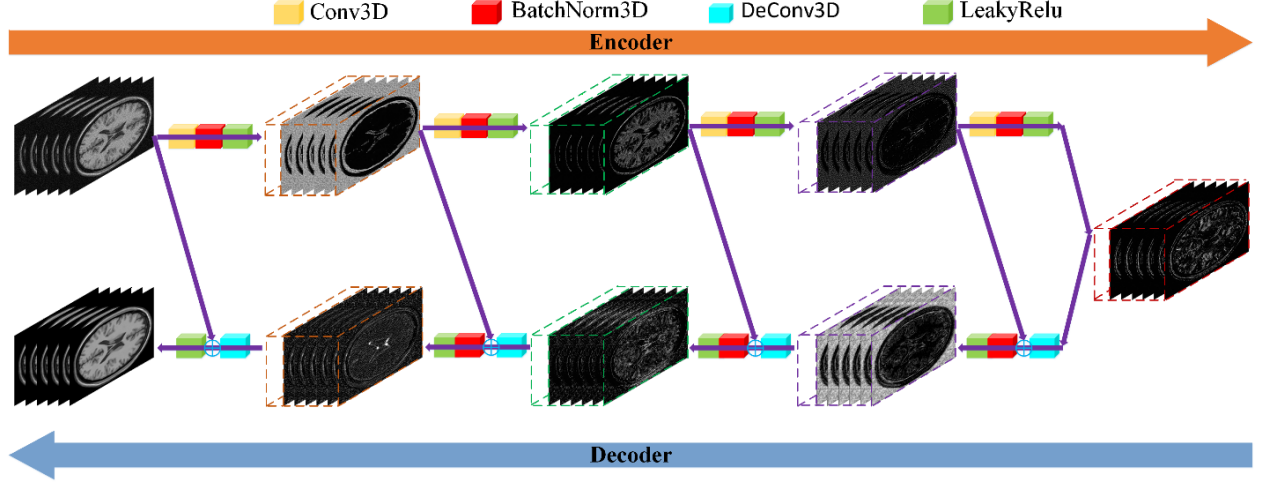


Fig. 2. The architecture of the generator network G

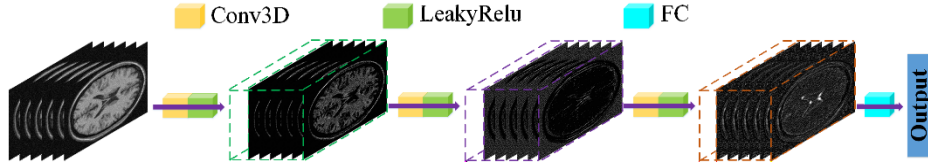


Fig. 3. The structure of the discriminator network D

The structure of discriminator D is illustrated in Fig.3. It has 3 convolutional layers with 32, 64 and 128 filter respectively. The kernel sizes are set to $3 \times 3 \times 3$ in all the convolution layers. The last layer is a fully-connected layer which has a single output to give the discriminant result.

We use a pre-trained VGG-19 network to extract the features. For more details, the readers can see the original reference [58]. Thanks to the power of transfer learning [59], there is no need to retrain the network with our target MR images.

3 Experiment

3.1 Datasets

To validate the performance of the proposed RED-WGAN, extensive experiments on both clinical and simulated datasets were carried out.

1) Clinical Data

For the clinical experiments, the well-known IXI dataset (<http://brain-development.org/ixi-dataset/>), which is collected from 3 different hospitals, was used. The detailed scanning configuration is given in the website mentioned above.

We randomly select 110 T1, T2 and PD-weighted brain image volumes respectively from Hammersmith dataset acquired from a Philips 3T scanner, which is a subset of IXI dataset. 100 image volumes are randomly selected as training

set, and the other 10 image volumes formed the testing set. It is well-known that deep learning based methods require a great deal of training samples, which is very difficult to be satisfied especially in clinics. To solve this problem, in this study, overlapped cubes are extracted from the samples to train the network. This method has been proved efficient that the perceptual differences can be better detected, and the number of samples significantly increases [38,60,61]. 50000 cubes with size of $32 \times 32 \times 6$ are acquired by a fixed sliding step.

2) Simulated Data

For simulated experiments, BrainWeb database (<http://brainweb.bic.mni.mcgill.ca/brainweb/>) was used. This dataset contains T1, T2 and PD-weighted brain images with size of $181 \times 217 \times 181$ with $1 \times 1 \times 1$ resolution. The network trained by the dataset from Hammersmith dataset was used. In the evaluation phase, we chose 6 continuous T1w slices from middle position of transverse plane as a test sample to evaluate the performance of compared methods.

3.2 Training Detail

To demonstrate the profits obtained by our proposed network architecture, two different networks were trained, including: RED-WGAN and CNN3D (RED-WGAN with only generator part and MSE loss) which can be approximately seen as an improved version of [48].

Both networks mentioned above were trained on T1, T2 and PD-weighted brain image cubes with specific noise level respectively. The parameters λ_1 , λ_2 and λ_3 were experimentally set to 1, 0.1 and $1e^{-3}$ according to the suggestion in [35,41]. Following the suggestions in [49], the penalty coefficient λ in Eq. (4) was set to 10. Adam was utilized to optimize the loss function [62] and the parameters for Adam were respectively set as $\alpha = 5e - 5, \beta_1 = 0.5, \beta_2 = 0.9$.

3.3 Evaluation methods

To validate the performance of the proposed RED-WGAN, three methods, including CNN3D, BM4D and PRI-NLM were compared. To evaluate the performance of these methods quantitatively, two quantitative metrics were employed. The first one is peak signal to noise ratio (PSNR) which considers the root mean square error (RMSE) between ground truth and denoised images. The PSNR is defined as:

$$\text{PSNR} = 20 \log_{10} \frac{255}{\sqrt{\frac{1}{mn} \sum_{i=0}^{m-1} \sum_{j=0}^{n-1} [I(i,j) - K(i,j)]^2}} \quad (10)$$

where I is $m \times n$ noise-free image and K is its noisy approximation. The second one is the structural similarity index

measure (SSIM) which is defined as follows:

$$\text{SSIM} = \frac{(2\mu_x\mu_{\hat{x}} + c_1)(2\sigma_{x\hat{x}} + c_2)}{(\mu_x^2 + \mu_{\hat{x}}^2 + c_1)(\sigma_x^2 + \sigma_{\hat{x}}^2 + c_2)} \quad (11)$$

where μ_x and $\mu_{\hat{x}}$ are the means of image x and \hat{x} , c_1 and c_2 are constants, σ_x and $\sigma_{\hat{x}}$ are variances and $\sigma_{x\hat{x}}$ is the covariance of x and \hat{x} .

3.4 Results

1) Clinical results

The average quantitative results of BM4D, PRI-NLM, CNN3D and RED-WGAN on T1w, T2w and PDw images with different noise levels from 1% to 15% with a step of 2% are illustrated in Tables I-III. It can be observed that the performances of DL based methods are significantly superior to the traditional denoising algorithms, such as BM4D and PRI-NLM on both PSNR and SSIM. For T1w images, the scores of RED-WGAN method are close to CNN3D method when

Table I

PSNR and SSIM measures of different methods on T1w images with different noise level

	1%	3%	5%	7%	9%	11%	13%	15%
Noise	39.2092 0.8325	29.2209 0.6007	24.6349 0.4964	21.6248 0.4242	19.3978 0.3667	17.6280 0.3186	16.1530 0.2771	14.8845 0.2417
BM4D	43.7217 0.9832	37.3037 0.9393	34.5095 0.9034	32.6762 0.8926	31.3338 0.8798	29.7973 0.8622	28.1597 0.8417	25.9018 0.8126
PRI-NLM	42.5101 0.9601	36.7709 0.9357	33.8254 0.8854	31.3052 0.7830	29.4420 0.7432	27.9812 0.6767	26.8905 0.6816	26.3974 0.6664
CNN3D	44.7101 0.9867	38.4564 0.9542	35.8638 0.9293	33.6071 0.9091	32.7940 0.9005	31.4896 0.8927	29.9069 0.8659	28.6901 0.8525
RED-WGAN	44.4336 0.9806	36.5281 0.9205	34.4664 0.8957	33.0387 0.8957	33.0367 0.9021	32.1459 0.8927	30.5995 0.8779	29.5566 0.8679

Table II

PSNR and SSIM measures of different methods on T2w images with different noise level.

	1%	3%	5%	7%	9%	11%	13%	15%
Noise	39.4202 0.8608	29.3326 0.6026	24.7211 0.4751	21.7165 0.3915	19.4976 0.3304	17.7243 0.2816	16.2557 0.2417	14.9919 0.2093
BM4D	44.0309 0.9758	37.7481 0.9238	34.8165 0.8856	32.5272 0.8582	30.1290 0.8222	28.0781 0.7935	24.6566 0.7315	20.7909 0.6267
PRI-NLM	43.1845 0.9615	37.2417 0.9320	33.9030 0.8494	31.3343 0.7550	30.0204 0.7380	28.1753 0.6749	26.4021 0.6005	26.0070 0.6042
CNN3D	44.9166 0.9757	38.5515 0.9210	36.2237 0.8972	34.4047 0.8833	33.0077 0.8657	31.9171 0.8511	30.7051 0.8274	29.9941 0.8197
RED-WGAN	44.9592 0.9769	38.5799 0.9223	36.2267 0.8972	34.5710 0.8838	33.0959 0.8672	31.9171 0.8511	30.7556 0.8294	29.7998 0.8181

Table III

PSNR and SSIM measures of different methods on PDw images with different noise level

	1%	3%	5%	7%	9%	11%	13%	15%
Noise	39.3873 0.8536	29.3073 0.5840	24.6963 0.4510	21.6903 0.3668	19.6796 0.3128	17.6862 0.2620	16.2160 0.2262	14.9550 0.1970
BM4D	44.7089 0.9787	38.6318 0.9266	36.0036 0.8898	34.2296 0.8703	32.6456 0.8547	30.9293 0.8342	29.0103 0.8124	26.3797 0.7857
PRI-NLM	43.8139 0.9721	37.6367 0.9058	34.5373 0.8520	32.4614 0.8131	31.2401 0.7900	29.3602 0.7250	28.3420 0.6946	27.333 0.6606
CNN3D	45.7124 0.9839	39.8149 0.9447	37.1052 0.8966	34.9915 0.8739	33.6963 0.8559	33.0781 0.8549	31.5944 0.8319	30.5857 0.8037
RED-WGAN	45.7125 0.9836	39.8201 0.9452	37.1031 0.8965	34.9867 0.8738	33.6870 0.8556	33.0561 0.8546	31.3285 0.8154	31.5303 0.8197

noise level is less than 7%. When the noise level goes up, RED-WGAN yields better performance than all the other methods. For T2w images, the PSNR and SSIM values of RED-WGAN are slightly better than all the other methods in most noisy levels. In Table III, although the results of CNN3D are slightly better than RED-WGAN, the differences are trivial.

Figs.4-6 provide a visual evaluation of different results on T1w, T2w and PDw brain images corrupted with 15% Rician noise selected from the testing set. It can be seen that all the methods can suppress the noise to varying degrees. However, BM4D and PRI-NLM suffer from obvious over-smoothing effect and distort some important details, which can be better

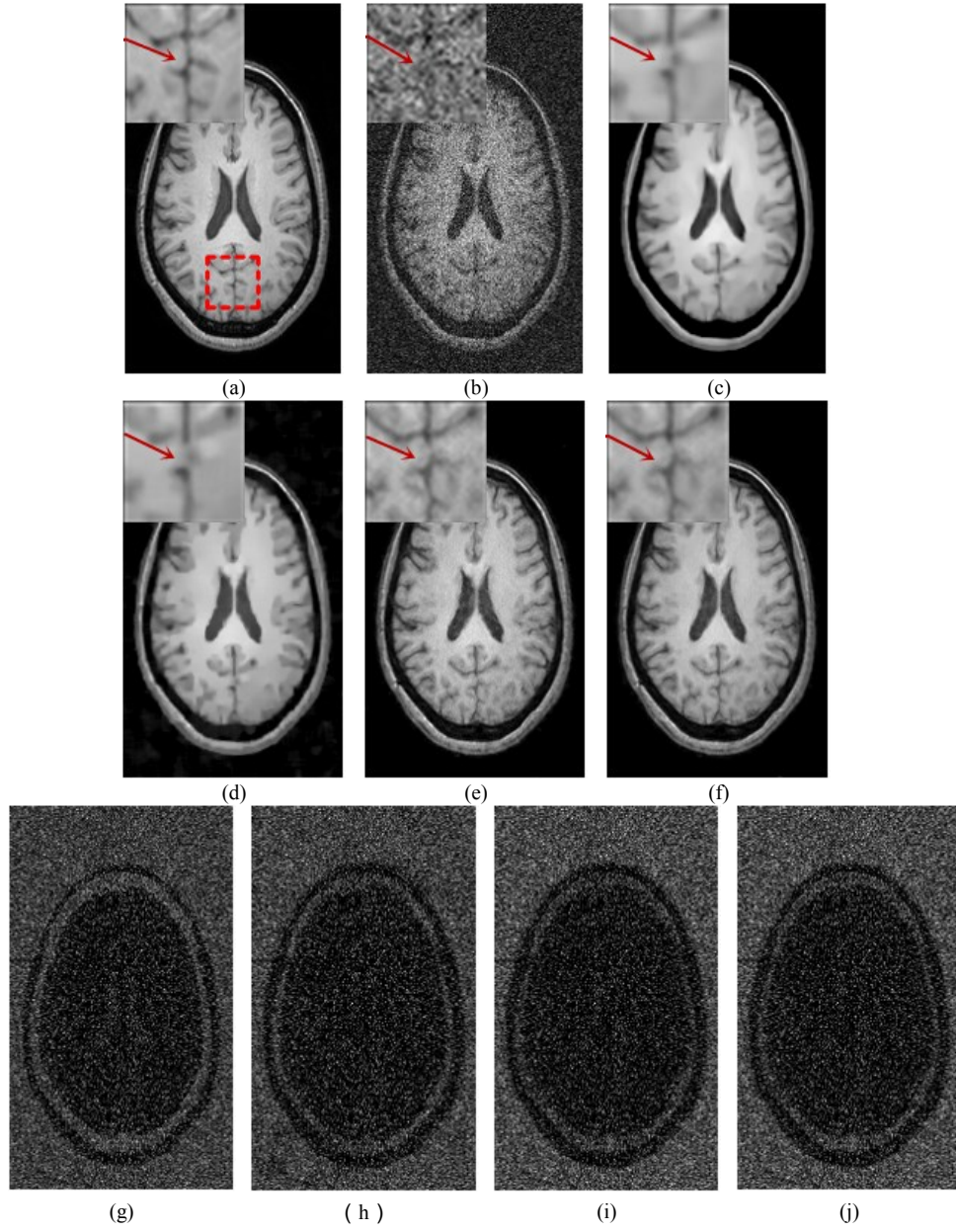


Fig.4. One denoised T1w example from testing set with 15% Rician noise. (a) Noise-free image, (b)Noisy image, (c) BM4D, (d) PRI-NLM, (e) CNN3D, (f) RED-WGAN, (g) Residual of BM4D, (h) Residual of PRI-NLM, (i) Residual of CNN3D, (j) Residual of RED-WGAN

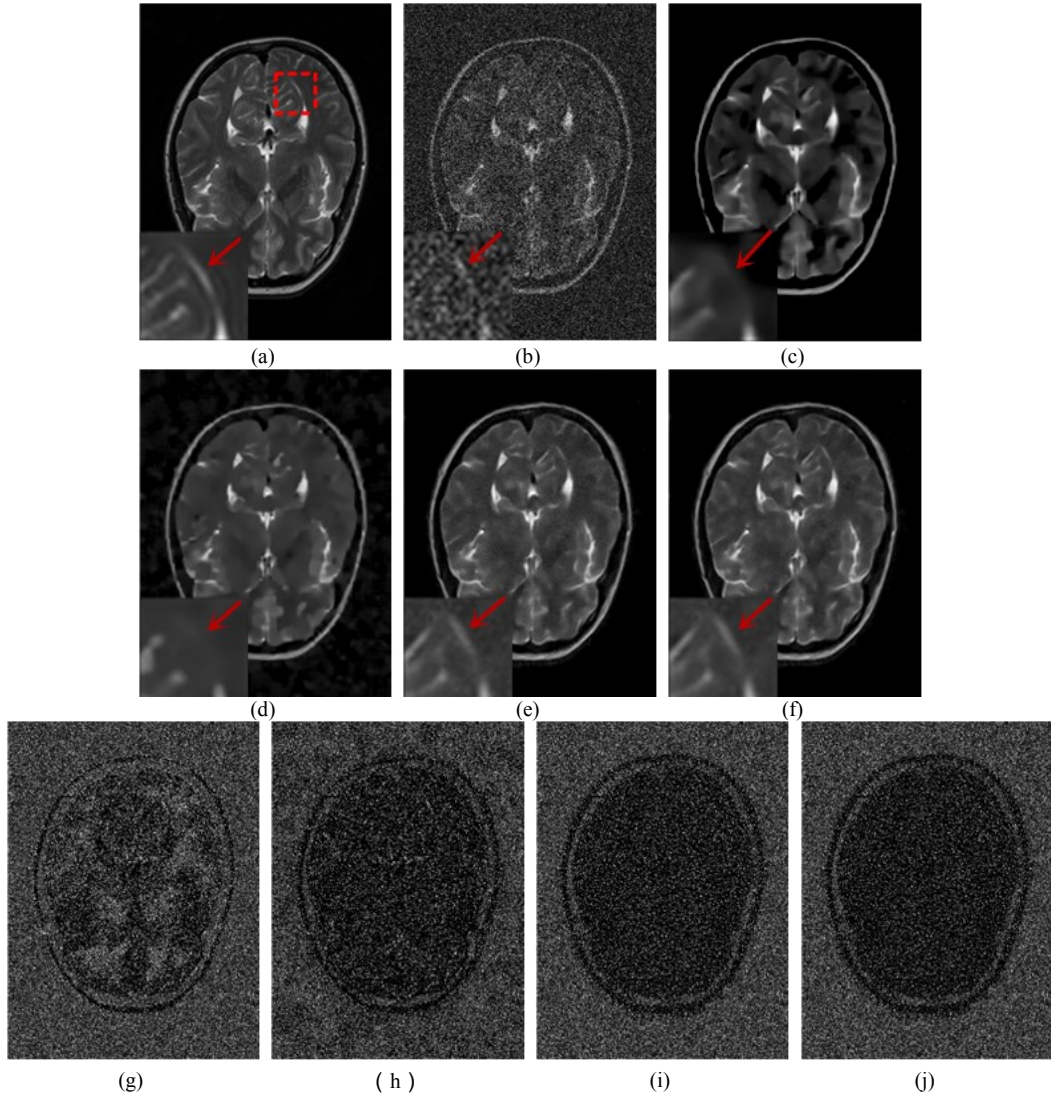


Fig.5. One denoised T2w example from testing set with 15% Rician noise. (a) Noise-free image, (b) Noisy image, (c) BM4D, (d) PRI-NLM, (e) CNN3D, (f) RED-WGAN, (g) Residual of BM4D, (h) Residual of PRI-NLM, (i) Residual of CNN3D, (j) Residual of RED-WGAN

Table IV
Quantitative results associated with different method for Figs.4, 5, and 6

Method	T1w		T2w		PDw		Average Exection Time(s)
	PSNR	SSIM	PSNR	SSIM	PSNR	SSIM	
Noise	14.7437	0.2603	14.6613	0.1797	14.2264	0.2164	
BM4D	27.0763	0.8354	22.9486	0.7173	25.7049	0.7776	5.73
PRI-NLM	28.2652	0.7901	26.0788	0.5612	26.3631	0.6897	4.16
CNN3D	29.1561	0.8742	29.8515	0.8254	28.3651	0.7893	0.17
RED-WGAN	30.0584	0.8892	29.9575	0.8351	31.1590	0.8624	0.16

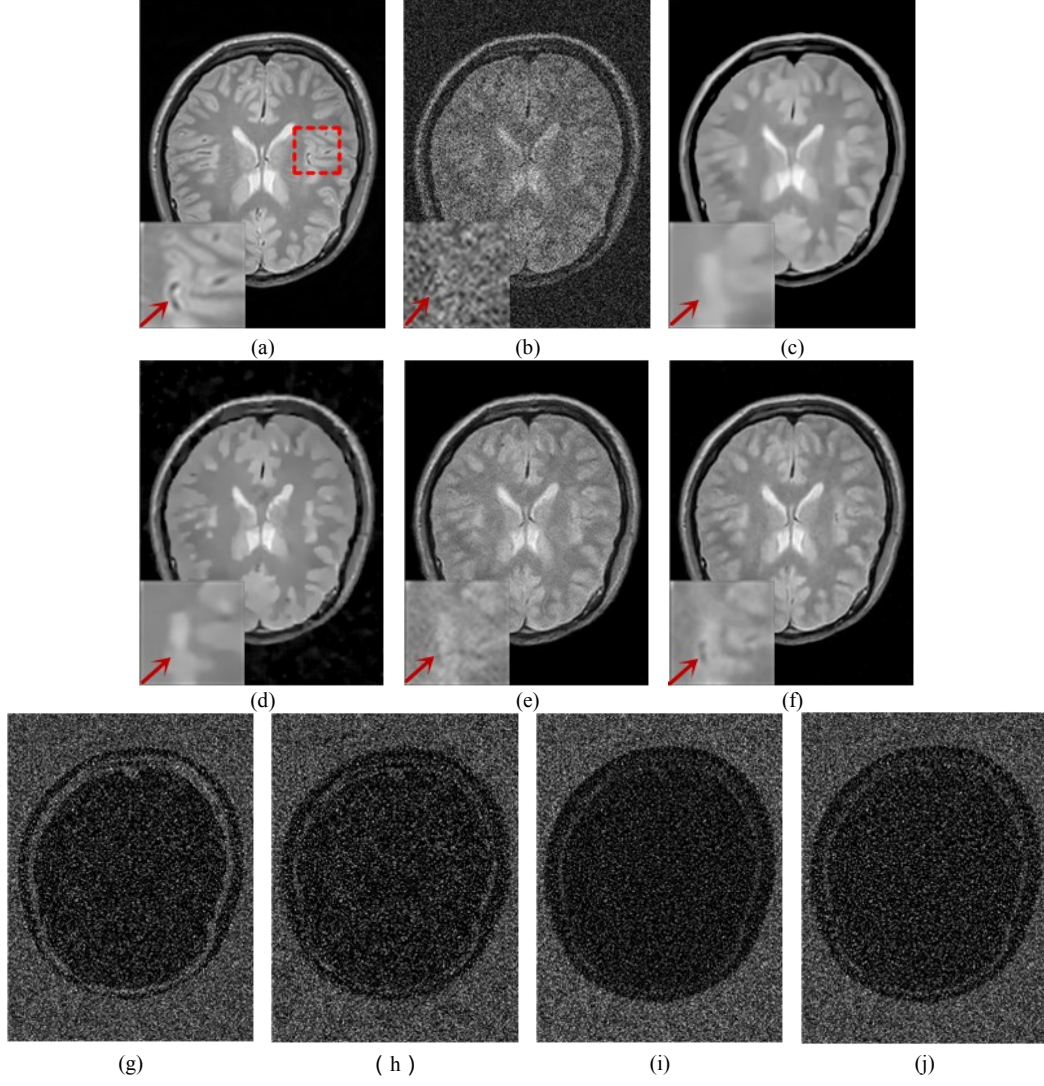


Fig.6. One denoised PDw example from testing set with 15% Rician noise. (a) Noise-free image, (b) Noisy image, (c) BM4D, (d) PRI-NLM, (e) CNN3D, (f) RED-WGAN, (g) Residual of BM4D, (h) Residual of PRI-NLM, (i) Residual of CNN3D, (j) Residual of RED-WGAN

sensed in Fig. 5 and 6. Both RED-WGAN and CNN3D avoid over-smoothing effect efficiently and preserve more structural details than BM4D and PRI-NLM. It also can be found that RED-WGAN outperforms CNN3D in noise suppression and obtains most consistent results to the reference images. The quantitative results from different methods for Figs. 4-6 are summarized in Table IV. The results suggest that RED-WGAN achieved best performance in terms of both PSNR and SSIM on all the modalities, which is coherent with the visual inspection. It also must be mentioned that although the quantitative results of RED-WGAN and CNN3D are close, the visual effect of RED-WGAN is significantly better than CNN3D in the enlarged regions. This benefit should be derived from the introduction of WGAN and combined loss function, which can efficiently generate the results more close to the original data distribution. In Table IV, we also demonstrated

the running times for different methods. It is clear that CNN3D and our proposed RED-WGAN is much faster than another two methods, This should benefit from that once the deep learning based method finishes training, forward propagation is very fast.

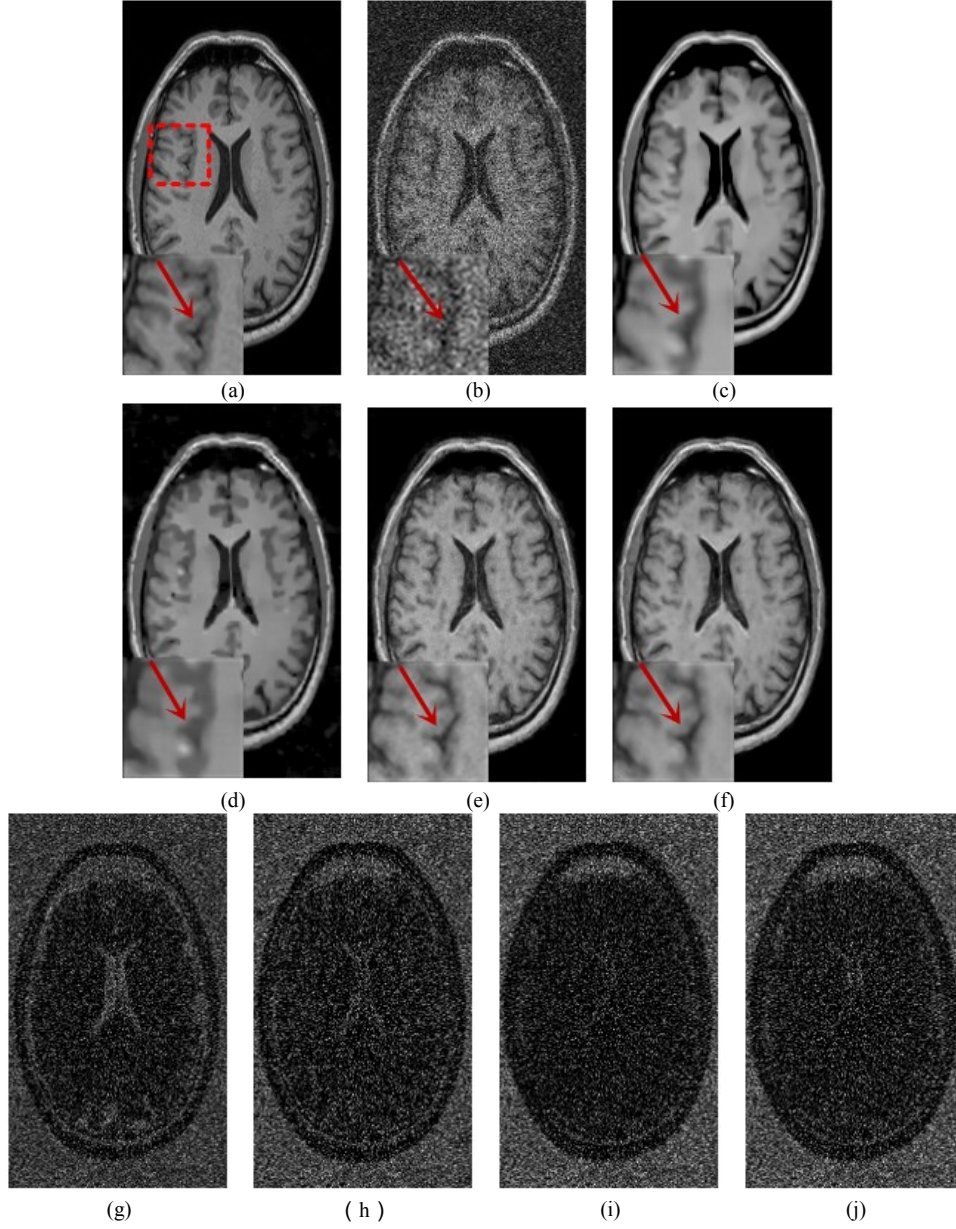


Fig.7. One denoised T1w example from Guys dataset with 15% Rician noise . (a) Noise-free image, (b) Noisy Image, (c)BM4D, (d) PRI-NLM, (e) CNN3D, (f) RED-WGAN, (g) Residual of BM4D, (h) Residual of PRI-NLM, (i) Residual of CNN3D, (j) Residual of RED-WGAN.

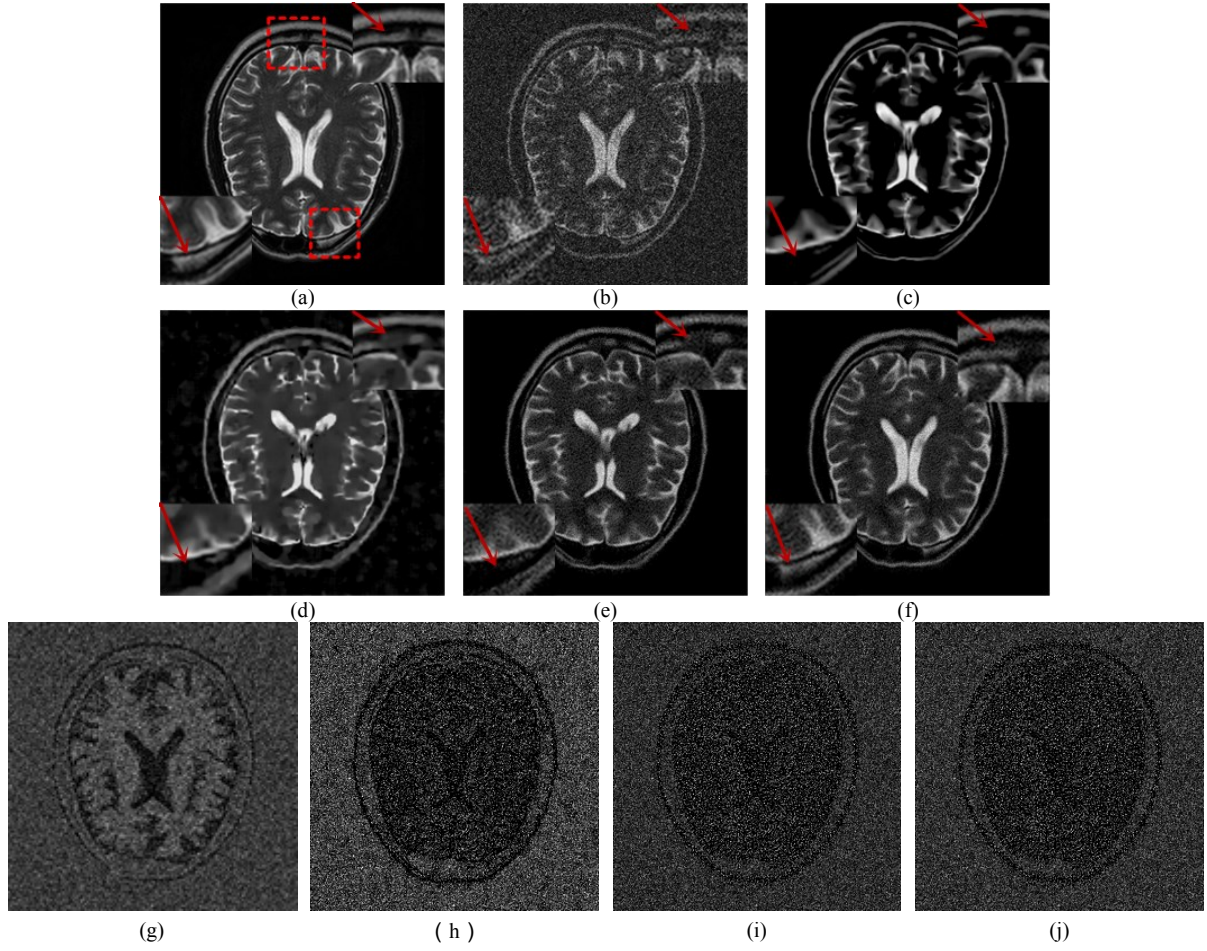


Fig.8. One denoised T2w example from Guys dataset with 15% Rician noise . (a) Noise-free image, (b) Noisy Image, (c)BM4D, (d) PRI-NLM, (e) CNN3D, (f) RED-WGAN, (g) Residual of BM4D, (h) Residual of PRI-NLM, (i) Residual of CNN3D, (j) Residual of RED-WGAN.

Table V
Quantitative results associated with different method outputs for Figs.7, 8 and 9

Method	T1w		T2w		PDw	
	PSNR	SSIM	PSNR	SSIM	PSNR	SSIM
Noise	14.5527	0.3020	14.2563	0.2183	14.1508	0.1874
BM4D	24.3476	0.8279	19.7854	0.6735	27.5299	0.8525
PRI-NLM	25.1755	0.7701	25.7850	0.6777	28.5738	0.6984
CNN3D	26.2868	0.8372	23.9495	0.7325	30.4959	0.8611
RED-WGAN	27.1845	0.8645	24.7837	0.7504	30.2283	0.8323

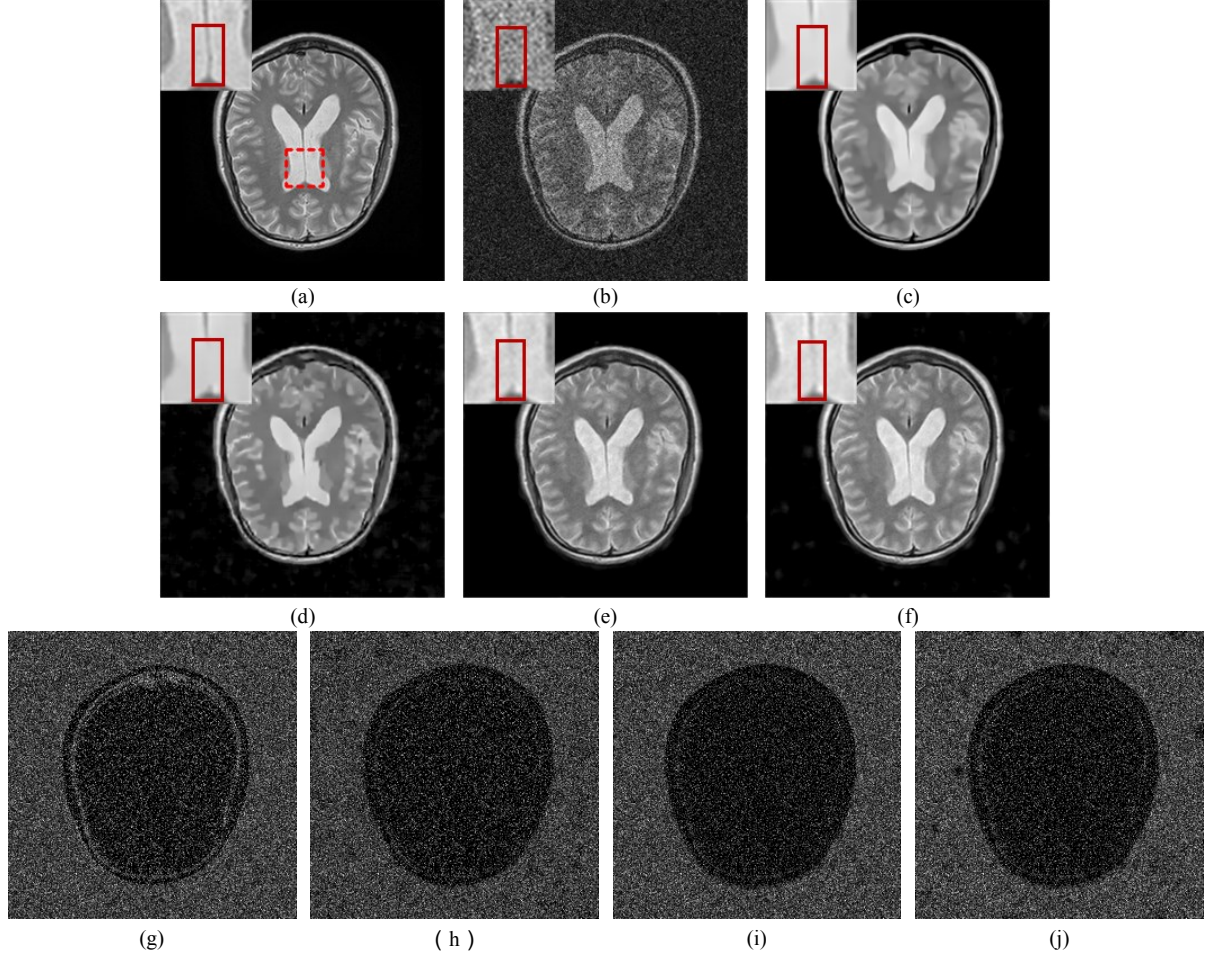


Fig.9. One denoised PDw example from Guys dataset with 15% Rician noise . (a) Noise-free image, (b) Noisy Image, (c)BM4D, (d) PRI-NLM, (e) CNN3D, (f) RED-WGAN, (g) residual of BM4D, (h) residual of PRI-NLM, (i) residual of CNN3D, (j) residual of RED-WGAN.

To further demonstrate the robustness of the proposed RED-WGAN, Guys dataset, which is another subset of IXI dataset, was included as testing set. Figs.7-9 show a denoised example for different modalities with different methods on Guys data with 15% Rician noise. Table V summarizes the corresponding quantitative results. It can be noticed that although the RED-WGAN and CNN3D were trained with a different training set, which has different scanning parameters, we still have satisfactory results in Figs.7-9. Most of the noise are efficiently removed and the structural details are better preserved in the result of RED-WGAN. It is also interesting to notice that PRI-NLM achieves good scores in PSNR, but its SSIM values are lower than other methods and the visual results are also unsatisfactory. This phenomenon can be seen as a proof that higher PSNR does not equal to better visual result. Some ROIs indicated by red dotted boxes were magnified to further demonstrate the differences produced by different methods. The residual images in Figs. 8 and 9 show that RED-WGAN well maintains the details and other methods lose the details to varying degrees.

2) Simulated results

One representative T1w result with 9% Rician noise from BrainWeb dataset is shown in Fig.10. In Fig.10, it is easy to notice that all the methods can eliminate most of the noise, but in the residual images, it can be seen that BM4D lost part of the structural details. From the enlarged regions, it is clear that RED-WGAN delivers better performance in terms of structure preservation than other methods. Meanwhile, RED-WGAN obtains best scores in both PSNR and SSIM.

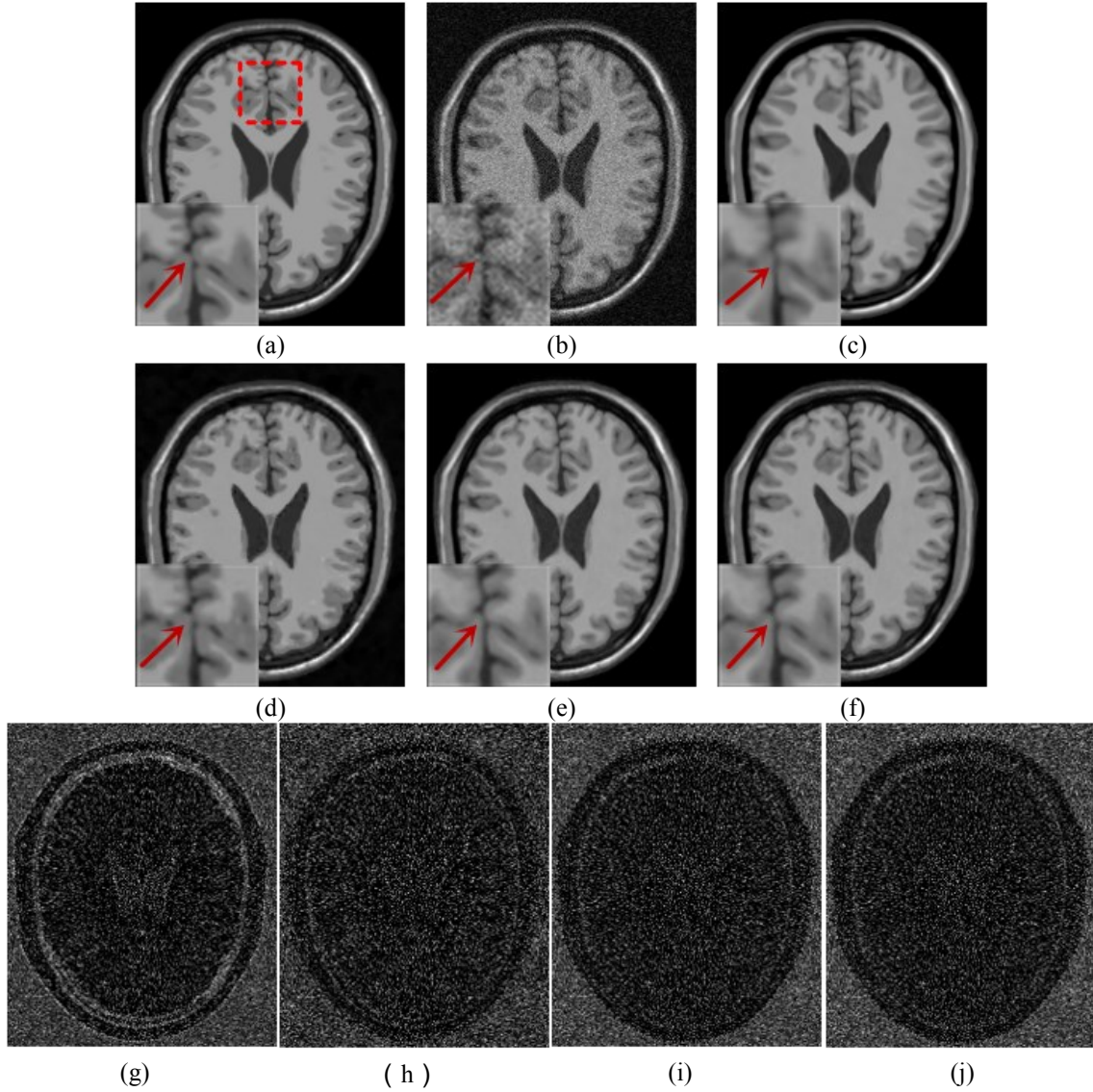


Fig.10. One denoised T1w example from BrainWeb dataset with 9% Rician noise. (a) Noise-free image, (b) Noisy image (PSNR=24.0697, SSIM=0.5847), (c) BM4D (PSNR=30.2730, SSIM=0.9335), (d) PRI-NLM (PSNR=32.4518, SSIM=0.8099), (e) CNN3D (PSNR=34.2789, SSIM=0.9665), (f) RED-WGAN (PSNR=34.7432, SSIM=0.9706), (g) Residual of BM4D, (h) Residual of PRI-NLM, (i) Residual of CNN3D, (j) Residual of RED-WGAN

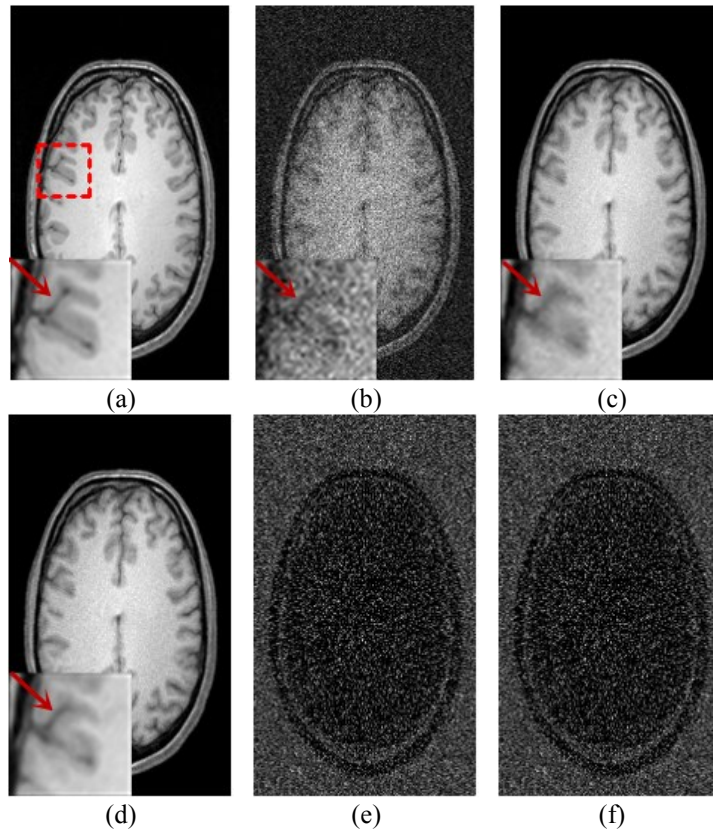


Fig.11. One denoised T1w example from testing set with 15% Rician noise . (a) Noise-free image, (b) Noisy Image, (c) WGAN-MSE, (d) RED-WGAN, (e) Residual of WGAN-MSE, (f) Residual of RED-WGAN.

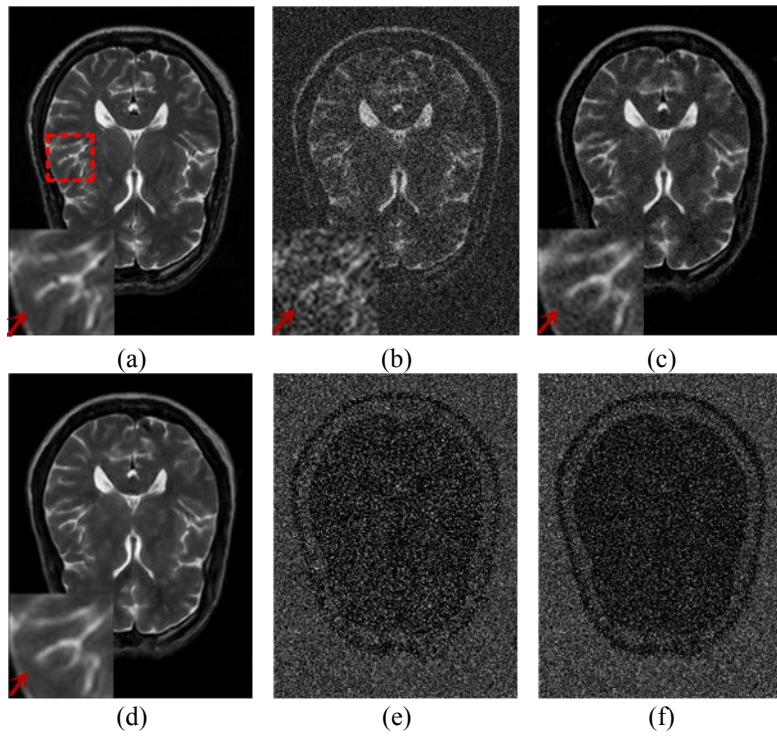


Fig.12. One denoised T2w example from testing set with 15% Rician noise . (a) Noise-free image, (b) Noisy Image, (c) WGAN-MSE, (d) RED-WGAN, (e) Residual of WGAN-MSE, (f) Residual of RED-WGAN.

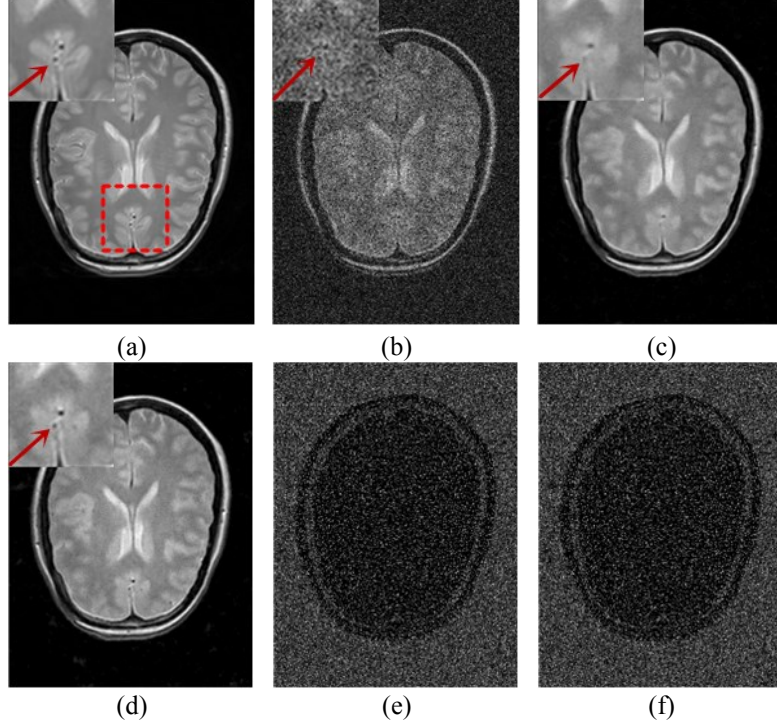


Fig.13. One denoised PDw example from testing set with 15% Rician noise . (a) Noise-free image, (b) Noisy Image, (c) WGAN-MSE, (d) RED-WGAN, (e) Residual of WGAN-MSE, (f) Residual of RED-WGAN.

Table VI
Quantitative results associated with different method outputs for Figs. 11, 12 and 13.

Method	T1w		T2w		PDw	
	PSNR	SSIM	PSNR	SSIM	PSNR	SSIM
Noise	15.0129	0.2698	15.0275	0.2108	14.6892	0.1966
CNN3D	28.9253	0.8280	26.7390	0.7212	31.7060	0.8449
RED-WGAN	29.8372	0.8743	29.3393	0.8156	32.2121	0.8309

3) Impact of perceptual loss

In this section, to sense the impact of perceptual loss, we compares RED-WGAN with it variant which has same structure as RED-WGAN, but only with MSE loss, and we denote it as WGAN-MSE. Figs.11-13 show an example of denoising results with both RED-WGAN and WGAN-MSE on T1w, T2w and PDw, respectively. From the result, it can be observed that the noise in WGAN-MSE are not well suppressed and some structures are blurred. On the other hand, RED-WGAN eliminates most noise while preserving the structural details better than WGAN-MSE. In Fig. 13, the blood vessel marked

by the red arrows is very hard to identify, while RED-WGAN well keeps it. Table VI shows the quantitative results for Figs.11-13. In Table VI, it can be seen that RED-WGAN outperforms WGAN-MSE in most cases, which is coherent with the visual results.

4 Discussions and Conclusion

In this paper, we propose a novel method based on Wasserstein generative adversarial network to remove the Rician noise in MR images while effectively preserve the structural details. This network aims to process 3D volume data using a 3D convolutional neural network. Except introduction of the WGAN framework, there are two more advantages for our method: the innovative generator structure and mixed weighted loss function. The generator is constructed with an auto-encoder structure, which symmetrically contains convolutional and deconvolutional layers, aided by residual structure. Another improvement of our method is the mixed loss function, which combines the MSE and perceptual loss with a weighted form.

The experimental results demonstrated that with the help of WGAN and perceptual loss, the CNN based method is significantly improved in both qualitative and quantitative aspects. Comparing to several state-of-art methods, including BM3D, PRI-NLM and CNN3D, our proposed RED-WGAN effectively avoid over-smoothing effect while preserves more details.

The computational cost of the deep learning based method is worth being mentioned. The training stage costs most of the computational time. Although the training procedure is usually carried out on GPU, it is still time-consuming. For our training set, when we alternately train the generator and discriminator networks, it takes about 40 minutes for each epoch. Although other methods, like BM4D and PRI-NLM, do not need to train, the running times of them are much longer than the DL based methods. In this paper, the average execution time for BM4D, PRI-NLM, CNN3D and RED-WGAN were 5.73, 4.16, 0.17 and 0.16 seconds for the clinical dataset respectively. In practice, the running time for DL based methods can be further reduce by using GPU for testing.

In conclusion, the results obtained in the paper are encouraging and efficiently demonstrate the potentials of deep learning based methods for MRI denoising. In the future, instead of training on a specific noise level, we will try to extend our method to a more general form for different noise levels. Furthermore, incorporating with image reconstruction method may be an interesting way.

Acknowledge

This work was supported in part by the National Natural Science Foundation of China under grants 61671312 and 61302028, the National Key R&D Program of China under grants 2017YFB0802300, the Science and Technology Project of Sichuan Province of China under grants 2018HH0070.

References

- [1] Mohan, J., Krishnaveni, V., Guo, Y., 2014. A survey on the magnetic resonance image denoising methods. *Biomed. Signal Process. Control* 9, 56-69.
- [2] Manjon, J., Carbonell-Caballero, J., Jj, Garcia-Marti, G., Marti-Bonmati, L., Robles, M., 2008. MRI denoising using non-local means. *Med. Image Anal.* 12, 514-523.
- [3] Zhang, X., Xu, Z., Jia, N., Yang, W., Feng, Q., Chen, W., Feng, Y., 2015. Denoising of 3D magnetic resonance images by using higher-order singular value decomposition. *Med. Image Anal.* 19, 75-86.
- [4] Mcveigh, E.R., Henkelman, R.M., Bronskill, M.J., 1985. Noise and filtration in magnetic resonance imaging. *Med. Phys.* 12, 586-591.
- [5] Perona, P., Malik, J., 1990. Scale-Space and Edge Detection Using Anisotropic Diffusion. *IEEE Trans. Pattern Anal. Mach. Intell.* 12, 629-639.
- [6] Krissian, K., Aja-Fernandez, S., 2009. Noise-Driven Anisotropic Diffusion Filtering of MRI. *IEEE Trans. Image Process.* 18, 2265-2274.
- [7] Nowak, R.D., 1999. Wavelet-based Rician noise removal for magnetic resonance imaging. *IEEE Trans. Image Process.* 8, 1408-1419.
- [8] Ma, J., Plonka, G., 2007. Combined Curvelet Shrinkage and Nonlinear Anisotropic Diffusion. *IEEE Trans. Image Process.* 16, 2198-2206.
- [9] Sijbers, J., den Dekker, A.J., Scheunders, P., Van, D.D., 1998. Maximum-likelihood estimation of Rician distribution parameters. *IEEE Trans. Med. Imaging* 17, 357-361.
- [10] Rajan, J., Veraart, J., Van Audekerke, J., Verhoye, M., Sijbers, J., 2012. Nonlocal maximum likelihood estimation method for denoising multiple-coil magnetic resonance images. *Magn. Reson. Imaging* 30, 1512-1518.
- [11] Gerig, G., Kübler, O., Kikinis, R., Jolesz, F.A., 1992. Nonlinear anisotropic filtering of MRI data. *IEEE Trans. Med. Imaging* 11, 221-232.
- [12] Samsonov, A.A., Johnson, C.R., 2004. Noise - adaptive nonlinear diffusion filtering of MR images with spatially

varying noise levels. *Magnetic Resonance in Medicine Official Journal of the Society of Magnetic Resonance in Medicine* 52, 798.

- [13] Pal, C., Das, P., Chakrabarti, A., Ghosh, R., 2017. Rician noise removal in magnitude MRI images using efficient anisotropic diffusion filtering. *Int. J. Imaging Syst. Technol.* 27, 248-264.
- [14] Yaroslavsky, L.P., Egiazarian, K.O., Astola, J.T., 2001. Transform domain image restoration methods: review, comparison, and interpretation. *Proceedings of SPIE - The International Society for Optical Engineering*, 155-169.
- [15] Anand, C.S., Sahambi, J.S., 2009. MRI denoising using bilateral filter in redundant wavelet domain, *TENCON 2008 - 2008 IEEE Region 10 Conference*, pp. 1-6.
- [16] Pizurica, A., Philips, W., Lemahieu, I., Acheroy, M., 2003. A versatile wavelet domain noise filtration technique for medical imaging. *IEEE Trans. Med. Imaging* 22, 323-331.
- [17] Hu, J., Pu, Y., Wu, X., Zhang, Y., Zhou, J., 2012. Improved DCT-based nonlocal means filter for MR images denoising. *Comput. Math. Method Med.*, 2012, (2012-3-7) 2012, 232685.
- [18] Bouhrara, M., Bonny, J.M., Ashinsky, B., Maring, M., Spencer, R., 2016. Noise Estimation and Reduction in Multispectral Magnetic Resonance Images. *IEEE Trans. Med. Imaging* 36, 181.
- [19] He, L., Greenshields, I.R., 2009. A nonlocal maximum likelihood estimation method for Rician noise reduction in MR images. *IEEE Trans. Med. Imaging* 28, 165-172.
- [20] Awate, S.P., Whitaker, R.T., 2007. Feature-preserving MRI denoising: a nonparametric empirical Bayes approach. *IEEE Trans. Med. Imaging* 26, 1242-1255.
- [21] Golshan, H.M., Hasanzadeh, R.P., Yousefzadeh, S.C., 2013. An MRI denoising method using image data redundancy and local SNR estimation. *Magn. Reson. Imaging* 31, 1206-1217.
- [22] Buades, A., Coll, B., Morel, J.M., 2005. A Non-Local Algorithm for Image Denoising, *Computer Vision and Pattern Recognition, 2005. CVPR 2005. IEEE Computer Society Conference on*, pp. 60-65 vol. 62.
- [23] Coupé, P., Yger, P., Prima, S., Hellier, P., Kervrann, C., Barillot, C., 2008. An optimized blockwise nonlocal means denoising filter for 3-D magnetic resonance images. *IEEE Trans. Med. Imaging* 27, 425-441.
- [24] Wiest-Daesslé, N., Prima, S., Coupé, P., Morrissey, S.P., Barillot, C., 2008. Rician noise removal by non-local means filtering for low signal-to-noise ratio MRI: applications to DT-MRI, *International Conference on Medical Image Computing and Computer-assisted Intervention*. Springer, pp. 171-179.
- [25] Hu, J., Zhou, J., Wu, X., 2016. Non-local MRI Denoising Using Random Sampling. *Magn. Reson. Imaging* 34, 990-999.

- [26] Manjón, J.V., Coupé, P., Buades, A., Louis, C.D., Robles, M., 2012. New methods for MRI denoising based on sparseness and self-similarity. *Med. Image Anal.* 16, 18-27.
- [27] Dabov, K., Foi, A., Katkovnik, V., Egiazarian, K., 2007. Image Denoising by Sparse 3-D Transform-Domain Collaborative Filtering. *IEEE Trans. Image Process.* 16, 2080-2095.
- [28] Maggioni, M., Katkovnik, V., Egiazarian, K., Foi, A., 2012. Nonlocal transform-domain filter for volumetric data denoising and reconstruction. *IEEE Trans. Image Process.* 22, 119-133.
- [29] Rajwade, A., Rangarajan, A., Banerjee, A., 2013. Image Denoising Using the Higher Order Singular Value Decomposition. *IEEE Trans. Pattern Anal. Mach. Intell.* 35, 849-862.
- [30] Girshick, R., 2015. Fast r-cnn, *Proceedings of the IEEE international conference on computer vision*, pp. 1440-1448.
- [31] He, K., Gkioxari, G., Dollár, P., Girshick, R., 2017. Mask r-cnn, *Computer Vision (ICCV), 2017 IEEE International Conference on.* IEEE, pp. 2980-2988.
- [32] He, K., Zhang, X., Ren, S., Sun, J., 2016. Deep residual learning for image recognition, *Proceedings of the IEEE conference on computer vision and pattern recognition*, pp. 770-778.
- [33] Long, J., Shelhamer, E., Darrell, T., 2015. Fully convolutional networks for semantic segmentation, *Proceedings of the IEEE conference on computer vision and pattern recognition*, pp. 3431-3440.
- [34] Ronneberger, O., Fischer, P., Brox, T., 2015. U-net: Convolutional networks for biomedical image segmentation, *International Conference on Medical image computing and computer-assisted intervention.* Springer, pp. 234-241.
- [35] Ledig, C., Theis, L., Huszár, F., Caballero, J., Cunningham, A., Acosta, A., Aitken, A.P., Tejani, A., Totz, J., Wang, Z., 2017. Photo-Realistic Single Image Super-Resolution Using a Generative Adversarial Network, *CVPR*, p. 4.
- [36] Zhang, K., Zuo, W., Chen, Y., Meng, D., Zhang, L., 2017. Beyond a gaussian denoiser: Residual learning of deep cnn for image denoising. *IEEE Trans. Image Process.* 26, 3142-3155.
- [37] Vincent, P., Larochelle, H., Lajoie, I., Bengio, Y., Manzagol, P.A., 2010. Stacked Denoising Autoencoders: Learning Useful Representations in a Deep Network with a Local Denoising Criterion. *J. Mach. Learn. Res.* 11, 3371-3408.
- [38] Dong, C., Chen, C.L., He, K., Tang, X., 2016. Image Super-Resolution Using Deep Convolutional Networks. *IEEE Trans. Pattern Anal. Mach. Intell.* 38, 295-307.
- [39] Dong, C., Chen, C.L., He, K., Tang, X., 2014. *Learning a Deep Convolutional Network for Image Super-Resolution.* Springer International Publishing.
- [40] Chen, H., Zhang, Y., Kalra, M.K., Lin, F., Chen, Y., Liao, P., Zhou, J., Wang, G., 2017. Low-Dose CT with a Residual Encoder-Decoder Convolutional Neural Network (RED-CNN). *IEEE Trans. Med. Imaging PP*, 1-1.

- [41] Yang, Q., Yan, P., Zhang, Y., Yu, H., Shi, Y., Mou, X., Kalra, M.K., Zhang, Y., Sun, L., Wang, G., 2017. Low-Dose CT Image Denoising Using a Generative Adversarial Network With Wasserstein Distance and Perceptual Loss. *IEEE Trans. Med. Imaging* 37, 1348-1357.
- [42] Li, H., Mueller, K., 2017. Low-Dose CT streak artifacts removal using deep residual neural network, *Proc. 14th Int. Meeting Fully Three-Dimensional Image Reconstruction Radiol. Nucl. Med.*, pp. 191-194.
- [43] Wang, S., Su, Z., Ying, L., Peng, X., Zhu, S., Liang, F., Feng, D., Liang, D., 2016. Accelerating magnetic resonance imaging via deep learning, *IEEE International Symposium on Biomedical Imaging*, pp. 514-517.
- [44] Xiang, L., Qiao, Y., Nie, D., An, L., Wang, Q., Shen, D., 2017. Deep Auto-context Convolutional Neural Networks for Standard-Dose PET Image Estimation from Low-Dose PET/MRI. *Neurocomputing* 267, 406-416.
- [45] Li, R., Zhang, W., Suk, H.I., Wang, L., Li, J., Shen, D., Ji, S., 2014. Deep Learning Based Imaging Data Completion for Improved Brain Disease Diagnosis, *International Conference on Medical Image Computing and Computer-Assisted Intervention*, pp. 305-312.
- [46] Xu, J., Gong, E., Pauly, J., Zaharchuk, G., 2017. 200x Low-dose PET Reconstruction using Deep Learning.
- [47] Jiang, D., Dou, W., Vosters, L., Xu, X., Sun, Y., Tan, T., 2018. Denoising of 3D magnetic resonance images with multi-channel residual learning of convolutional neural network. *Japanese Journal of Radiology*, 1-9.
- [48] Andersen, A.H., 1996. On the Rician distribution of noisy MRI data. *Magn. Reson. Med.* 36, 331-333.
- [49] Goodfellow, I.J., Pouget-Abadie, J., Mirza, M., Xu, B., Warde-Farley, D., Ozair, S., Courville, A., Bengio, Y., 2014. Generative adversarial nets, *International Conference on Neural Information Processing Systems*, pp. 2672-2680.
- [50] Isola, P., Zhu, J.Y., Zhou, T., Efros, A.A., 2017. Image-to-Image Translation with Conditional Adversarial Networks, *IEEE Conference on Computer Vision and Pattern Recognition*, pp. 5967-5976.
- [51] Kataoka, Y., Matsubara, T., Uehara, K., 2016. Image generation using generative adversarial networks and attention mechanism, *Ieee/acis International Conference on Computer and Information Science*, pp. 1-6.
- [52] Arjovsky, M., Bottou, L., 2017. Towards Principled Methods for Training Generative Adversarial Networks.
- [53] Arjovsky, M., Chintala, S., Bottou, L., 2017. Wasserstein GAN.
- [54] Gulrajani, I., Ahmed, F., Arjovsky, M., Dumoulin, V., Courville, A., 2017. Improved Training of Wasserstein GANs.
- [55] Johnson, J., Alahi, A., Li, F.F., 2016. Perceptual Losses for Real-Time Style Transfer and Super-Resolution. 694-711.
- [56] Bruna, J., Sprechmann, P., Lecun, Y., 2015. Super-Resolution with Deep Convolutional Sufficient Statistics. *Computer Science*.
- [57] Gatys, L.A., Ecker, A.S., Bethge, M., 2015. Texture Synthesis Using Convolutional Neural Networks. 70, 262-270.

- [58] Simonyan, K., Zisserman, A., 2014. Very Deep Convolutional Networks for Large-Scale Image Recognition. Computer Science.
- [59] Pan, S.J., Yang, Q., 2010. A Survey on Transfer Learning. IEEE Trans. Knowl. Data Eng. JCR Abbrev: IEEE T KNOWL DATA EN 22, 1345-1359.
- [60] Xie, J., Xu, L., Chen, E., 2012. Image denoising and inpainting with deep neural networks, International Conference on Neural Information Processing Systems, pp. 341-349.
- [61] Jain, V., Seung, H.S., 2008. Natural image denoising with convolutional networks, International Conference on Neural Information Processing Systems, pp. 769-776.
- [62] Kinga, D., Adam, J.B., 2015. A method for stochastic optimization, International Conference on Learning Representations (ICLR).